Eur. Phys. J. Plus (2026) 141:8
https://doi.org/10.1140/epjp/s13360-025-07203-1

THE EUROPEAN PHYSICAL JOURNAL PLUS

Regular Article

Evaporation dynamics and observational aspects of Bardeen–Kiselev black holes in AdS spacetimes

Shahid Chaudhary[1,2,a], **Muhammad Danish Sultan**[3,b], **Talha Anwar**[10,c], **A. F. Abd EI-Rehim**[4], **Farruh Atamurotov**[5,6,7], **Muhammad Hadi**[8], **M. A. Sayed**[8], **Ali M. Mubaraki**[9]

[1] Department of Natural Sciences and Humanities, University of Engineering and Technology Lahore, New Campus, Lahore, Pakistan
[2] Research Center of Astrophysics and Cosmology, Khazar University, 41 Mehseti Street, 1096 Baku, Azerbaijan
[3] Department of Physics, Durham University, Durham, UK
[4] Physics Department, Faculty of Science, King Khalid University, P.O. Box 9004, 61413 Abha, Saudi Arabia
[5] Kimyo International University in Tashkent, Shota Rustaveli Str. 156, 100121 Tashkent, Uzbekistan
[6] University of Tashkent for Applied Sciences, Str. Gavhar 1, 100149 Tashkent, Uzbekistan
[7] Tashkent State Technical University, 100095 Tashkent, Uzbekistan
[8] Department of Physics, Faculty of Science, King Khalid University, Abha, Saudi Arabia
[9] Department of Mathematics and Statistics, College of Science, Taif University, P.O. Box 11099, 21944 Taif, Saudi Arabia
[10] Department of Mathematics, COMSATS University Islamabad, Islamabad 45550, Pakistan

Received: 26 June 2025 / Accepted: 12 December 2025

Abstract In this paper, we explore the dynamics, thermodynamics, and observational features of the Bardeen–Kiselev black hole in AdS spacetime, motivated by the need to resolve curvature singularities and incorporate the influence of dark energy in strong gravity regimes. By coupling nonlinear electrodynamics with a quintessence field, the Bardeen–Kiselev–AdS solution provides a physically regular and rich framework to study modified black hole behavior. We first investigate the Hawking evaporation process and show that magnetic monopole charge induces a repulsive core that halts complete evaporation, resulting in a stable remnant which is significant deviation from traditional singular black hole models. In contrast, the Kiselev–AdS black hole without magnetic charge undergoes total mass loss, illustrating the crucial role of nonlinear electrodynamic effects. Next, we analyze the evolution of scalar perturbations and find that increasing the quintessence parameter enhances wave dissipation, while higher magnetic charge improves perturbative stability through deeper effective potentials. To further understand quantum effects, we compute rigorous bounds on the greybody factors using the Visser–Boonserm method and demonstrate that quintessence suppresses radiation transmission, whereas magnetic charge amplifies it, modifying the observable Hawking spectrum. Additionally, we examine the black hole shadow and find that quintessence shrinks the apparent shadow size, while magnetic charge enlarges it due to modifications in the photon sphere geometry. Lastly, employing the Novikov–Thorne model, we simulate the accretion disk images and show how parameters like q, c, and observer inclination θ impact the disk s shape, and relativistic lensing features.

1 Introduction

General relativity (GR) successfully predicts and explains various astrophysical phenomena [1], with black holes (BHs) being one of its most significant predictions [2]. Owing to their unique causal structure, BHs possess a boundary called event horizon, beyond which any particle or wave that crosses cannot escape. In recent years, BH research has gained increasing importance. Two significant events that have advanced BH research are observation of gravitational waves (GWs) by LIGO [3, 4], and image of a BH's surrounding environment captured by event horizon telescope collaboration [5, 6]. While these experiments mark major breakthroughs, the observation of a shadow or gravitational ringdown is not conclusive proof of a BH solution [7]. Besides GR, also predicts other possible solutions, such as wormholes [8, 9], boson stars [10], black bounces [11, 12], and regular BHs [13, 14], among others [15]. In BHs, the issue of singularity emerger, regions in spacetime where geodesics are disrupted [16]. This occurrence might signal a limitation of the theory, as it is based on classical gravity. A quantum theory can potentially resolve the singularity problem [17]. There are also alternative approaches aimed at addressing the singularity problem. One such alternative is the concept of a regular BH, which is free of singularity. The regular BH was given by Bardeen [18, 19]. In recent years, the regular BH has expanded significantly, with numerous proposed models and analyses of their properties [20–22]. Another notable development is

[a] e-mails: shahidpeak00735@gmail.com; drshahid.ch@uet.edu.pk
[b] e-mail: 4847.m.danishsultan@gmail.com
[c] e-mail: talha@cui.edu.pk (corresponding author)

Published online: 04 January 2026

that within the framework of GR, these solutions are not solely characterized by coupling with nonlinear electrodynamics, which necessitates additional matter [12, 15]. Bronnikov and collaborators also introduced solution with structure resembling black bounce, called black universe [23]. Numerous studies have since emerged on black bounces, exploring aspects such as quasinormal modes, shadows, absorption, and other related phenomena [24, 25].

In 1974, using quantum field theory in curved spacetime, Hawking demonstrated that quantum mechanical effects enable BHs emit particles, a phenomenon called Hawking radiation [26, 27]. Hawking radiation plays a pivotal role in connecting quantum field theory with gravitational physics, and is widely regarded as a key phenomenon for probing the quantum nature of spacetime. Through this process, black holes continuously emit thermal particles, resulting in a gradual decrease in their mass, which in turn leads to the well-known information loss puzzle [28]. This quantum emission framework allows one to compute the radiative energy flux and estimate the characteristic evaporation timescale of a black hole [29]. Notably, the evaporation time diverges for black holes with arbitrarily large initial masses, implying that extremely massive black holes would require an infinite amount of time to evaporate completely. Similar considerations extend to more general geometries, including rotating and electrically charged black holes [30], where analogous quantum radiation mechanisms govern their thermodynamic evolution.

Since the first detection of GWs, over 90 GW events-originating from mergers of compact objects, like as BHs or neutron stars captured by the LIGO collaborations [31]. More advanced GWs detectors are being developed [32], including Cosmic Explorer [33], the Einstein Telescope [34], LISA [35], Tian Qin [36], Taiji [37], and DECIGO [38]. This has sparked the study of BH quasinormal modes (QNM) [39, 40] and the influence of dark matter on gravitational waves [41, 42], among other related phenomena. Gravitational waves produced during the ringdown phase following a coalescence, when a BH has just formed, can be understood as a linear combination of QNM of newly formed BH. These waves are typically analyzed using perturbation theory [43, 44]. The QNMs of like perturbations, including scalar, vector (electromagnetic), and tensor (gravitational) modes, have been widely investigated in both and various modified gravity theories. For further details, readers are referred to [45, 46].

Greybody factors characterize the modification of Hawking radiation as it propagates through the curved spacetime surrounding a black hole, effectively measuring the likelihood that emitted particles overcome the gravitational potential barrier. In the framework of classical general relativity, black holes act as perfect absorbers and do not emit radiation [47]. However, once quantum effects are taken into account, black holes emit thermal quanta the phenomenon known as Hawking radiation. As these quanta propagate outward, they scatter off the black hole's effective potential, leading to a partial transmission of particles to infinity and a partial reflection back toward the horizon. The resulting deviations from a perfect blackbody spectrum are encoded in the greybody factors, making them essential for understanding the observable properties of black hole radiation. Therefore, spectrum detected by observer varies from that of standard blackbody spectrum. A BH's GF measures the deviation from pure blackbody radiation [48]. There are several methods to obtain GF, including establishing bounds for coefficients in potential scattering.

BHs continue to serve as natural laboratories for exploring the profound interplay between gravity, quantum theory, and high-energy astrophysics. Traditional BH solutions in general relativity, while elegant, are often plagued by singularities regions where physical quantities diverge and predictability breaks down. To address this, regular BH models such as the Bardeen solution have emerged, removing central singularities by coupling gravity to nonlinear electrodynamics. Concurrently, the Kiselev model introduces a surrounding quintessence field to account for the effects of dark energy in the BH environment, enabling the study of exotic matter interactions in strong gravitational regimes. The fusion of these two frameworks in the Bardeen–Kiselev–(A)dS BH yields a compelling setting for deeper investigations. This hybrid model not only regularizes singularities but also captures the influence of quintessential dark energy and a negative cosmological constant, making it relevant for both theoretical insights and astrophysical observations in an (A)dS context.

The rapid progress in gravitational wave observations and the development of very high-resolution black hole imaging techniques, such as those employed by the Event Horizon Telescope, it becomes essential to understand how such complex matter-energy configurations modify observable phenomena like Hawking radiation, BH shadows, greybody spectra, and disk images. This study is therefore driven by the urgent need to understand how magnetic monopole charge and quintessence fields impact the thermodynamics, radiation, and stability of BHs. By analyzing evaporation behavior, perturbation dynamics, GF bounds, and accretion disk images within the Bardeen–Kiselev–(A)dS framework, we aim to provide novel predictions that can inform and possibly be tested by future observations. Our results not only enhance the theoretical foundations of regular BHs in modified gravity settings but also shed light on potential mechanisms of BH remnant formation and information preservation critical topics in quantum gravity and the (A)dS/CFT correspondence.

The paper organize as, In Sect. 2, we provide brief review of Bardeen–Kiselev (A)dS BH. In Sect. 3, we investigate Hawking evaporation of Bardeen–Kiselev BH in (A)dS spacetimes. In Sect. 4, we study perturbations of Bardeen–Kiselev BH in (A)dS spacetimes. In Sect. 5, we discuss GFs onto Bardeen–Kiselev (A)dS BH. In Sect. 6, we investigate Shadows of Bardeen–Kiselev (A)dS BH. In Sect. 7, we study accretion disk around Bardeen–Kiselev BH. In Sect. 8, we conclude our findings.

2 Bardeen–Kiselev solution with cosmological constant

The Bardeen–Kiselev solution with a cosmological constant represents a novel and physically rich BH model that combines several key features. Regular BHs (no singularity at the center) via the Bardeen solution, dark energy effects through the Kiselev component,

modeled using a quintessence field, embedding in asymptotically (Anti)-de Sitter (AdS/dS) spacetime via the cosmological constant. Together, this creates a BH solution relevant for both theoretical studies and astrophysical applications. The observational implications apply only to the dS case, while the AdS case is considered for theoretical completeness. We use the notation (A)dS throughout the relevant part of the manuscript to reflect the theoretical consideration of both asymptotics, while explicitly noting that only the dS sector has potential cosmological relevance. The Bardeen solution introduces a magnetic monopole via nonlinear electrodynamics, eliminating the central singularity. This makes the BH regular everywhere, aligning with attempts to resolve singularities in classical general relativity. It offers a more physically acceptable BH model, avoiding breakdowns in spacetime geometry. On the other hand, the Kiselev component introduces a surrounding quintessential field, characterized by an equation of state parameter. This models the influence of dark energy near the BH. It allows investigation of how cosmic acceleration and exotic matter fields affect BH thermodynamics, stability, and observable features. We consider BH solution in the framework of Bardeen–Kiselev BH with cosmological constant. The general structure of these models is characterized by

$$\mathrm{d}s^2 = f(r)\mathrm{d}t^2 - f(r)^{-1}\mathrm{d}r^2 - \left(\mathrm{d}\theta^2 + \sin^2\theta\mathrm{d}\phi^2\right)r^2. \tag{1}$$

The action in the theory is of the form [49]

$$S = \int \mathrm{d}^4x\sqrt{-g}[2\Lambda + R + L(\mathcal{F})], \tag{2}$$

were, curvature scalar is R, cosmological constant is Λ, and $L(\mathcal{F})$ yields nonlinear Lagrangian of the electromagnetic theory. This Lagrangian is a nonlinear function of electromagnetic scalar $\mathcal{F} = F^{\mu\nu}F_{\mu\nu}$, where $F^{\mu\nu}$ is the Maxwell–Faraday tensor. The only non-zero component of $F_{\mu\nu}$ [50] in the context of magnetically charged spherically symmetric spacetime is $F_{23} = q\sin\theta$, and scalar $\mathcal{F}$ is $\mathcal{F} = \frac{2q}{r^4}$, where q is magnetic charge. Let us assume Lagrangian [51, 52]

$$L(\mathcal{F}) = \frac{24\sqrt{2}Mq^2}{\kappa^2\left(\sqrt{\frac{2q^2}{\mathcal{F}}} + 2q^2\right)^{5/2}} - \frac{6\omega c(\frac{2\mathcal{F}}{q^2})^{3/4(\omega+1)}}{\kappa^2}. \tag{3}$$

where c is quintessence parameter and when $c \to 0$, it reduces to Bardeen solution. ω is equation of state parameter, M represents mass of BH. In the limit $\mathcal{F} \to 0$, we have

$$L(\mathcal{F}) \approx -\frac{6c2^{3/4(\omega+1)}\omega\mathcal{F}^{\frac{3(\omega+1)}{4}}F^{3(\omega+1)/4}}{\kappa^2(q^2)^{\frac{3}{4}(\omega+1)}} + \frac{12\sqrt[4]{2}\mathcal{F}\mathcal{F}^{1/4}m}{\kappa^2\sqrt[4]{q^2}} + O\left(\mathcal{F}\mathcal{F}^{3/4}\right). \tag{4}$$

When $\omega = 1/3$, this results in

$$L(\mathcal{F}) \approx -\frac{4c\mathcal{F}}{\kappa^2q^2} + \frac{12\sqrt[4]{2}\mathcal{F}\mathcal{F}^{1/4}m}{\kappa^2\sqrt[4]{q^2}} + O\left(\mathcal{F}\mathcal{F}^{3/4}\right), \tag{5}$$

Thus, very small values of $\mathcal{F}$ result in dominance of the linear term

$$\mathcal{F} \approx L(\mathcal{F}), \mathcal{F} \to 0. \tag{6}$$

This equation is actually the Maxwell weak field limit [53, 54]. It means that behavior of electromagnetism in Maxwell limit is almost akin to Maxwell theory. Einstein equations in the presence of cosmological constant are of the form

$$R_{\mu\nu} - \frac{1}{2}g_{\mu\nu}R + \Lambda g_{\mu\nu} = \kappa^2T_{\mu\nu}. \tag{7}$$

Utilizing the stress–energy tensor for nonlinear electrodynamics, we get

$$T_{\mu\nu} = g_{\mu\nu}L(\mathcal{F}) - \frac{\mathrm{d}L}{\mathrm{d}\mathcal{F}}F_{\mu}{}^{\alpha}F_{\nu\alpha}, \tag{8}$$

and solution of the Einstein equations gives us metric function

$$f(r) = 1 - 2cr^{-3\omega-1} - \frac{2Mr^2}{(q^2+r^2)^{3/2}} + \frac{r^2}{l^2}. \tag{9}$$

For the limiting case without quintessence ($c \to 0$), the Bardeen solution is recovered while ($q \to 0$) without magnetic charge it leads to the Kiselev solution [55]. The study of Bardeen–Kiselev de Sitter BH is of significant theoretical and observational interest. This class of solutions combines the features of the magnetically charged regular Bardeen BH with those of the Kiselev BH, which is surrounded by quintessence. To gain a deeper understanding of the physical properties and observational signatures of the Bardeen–Kiselev de Sitter BH, it is essential to explore several key phenomena associated with it. Horizons can be obtained by solving $f(r) = 0$. Due to the complexity of the metric function, analytic solutions are not possible; therefore, we obtain numerical solutions for the horizons. The temperature of BH can determined by using surface gravity as [56]

$$T_k = \frac{\kappa}{2\pi}, \tag{10}$$

here

$$\kappa = \left.\frac{f'(r)}{2}\right|_{r=r_+}, \tag{11}$$

represent surface gravity and r_+ manifest event horizon radius (outer radius). So, we get

$$T_k = \frac{1}{4\pi}\left[(6c\omega r_+^{-3\omega-2} + 2cr_+^{-3\omega-2}) + 2Mr_+\left(r_+^2 - 2q^2\right)\left(q^2 + r_+^2\right)^{-5/2} + \frac{2r_+}{l^2}\right]. \tag{12}$$

The first law of thermodynamics is defined as [57, 58]

$$\mathrm{d}M = T_H \mathrm{d}S + \Phi \mathrm{d}q + V\mathrm{d}P. \tag{13}$$

Here, M denotes energy, F represents magnetic potential, and P shows pressure, which is defined as

$$P = -\frac{\Lambda}{8\pi}, \tag{14}$$

and entropy of the system is S. According to area law [59]

$$S = \frac{A}{4} = \pi r_+^2, \tag{15}$$

where A is the area of the BH. We can determine M by using the condition $f(r_+) = 0$, which yields

$$M = -\frac{1}{6}\left(q^2 + r_+^2\right)^{3/2} r_+^{-3\omega-3}\left(6c - \frac{3}{l^2}r_+^{3\omega+3} - 3r_+^{3\omega+1}\right). \tag{16}$$

It is worth noting that the above expression for the BH mass incorporates the effects of both the nonlinear electromagnetic charge and the surrounding quintessence field. In particular, the term involving $(q^2+r_+^2)^{3/2}$ encapsulates the Bardeen regularization contribution arising from nonlinear electrodynamics. Meanwhile, the term proportional to the parameter c characterizes the influence of the Kiselev quintessence fluid, modifying the mass profile in a manner dependent on the equation of state parameter ω. This modification reflects how the external matter distribution affects the gravitational structure of the spacetime. Furthermore, the contribution proportional to r_+^3/l^2 demonstrates the interplay with the AdS curvature scale l, consistent with the extended phase-space interpretation where the cosmological constant acts as a thermodynamic pressure.

3 Hawking evaporation of Bardeen–Kiselev black hole in AdS spacetimes

The analysis of Hawking radiation plays a crucial role in connecting BH physics with quantum field theory. For the Bardeen–Kiselev black hole, studying the Hawking evaporation process enables us to understand how the regular geometry affects BH thermodynamics, the lifetime of the BH, and possible remnants. The mass of BH M behaves like a monotonically decreasing function of time t due to Hawking radiation when an absorbing boundary condition is incorporated. It is assumed that all ejected particles travel along null geodesics under the geometric optics approximation. In this scenario, the equation governing the motion of these massless particles is given by

$$\left(\frac{\mathrm{d}r}{\mathrm{d}\lambda}\right)^2 = -J^2\left(\frac{f(r)}{r^2}\right) + E^2, \tag{17}$$

here $E = f(r)\frac{\mathrm{d}t}{\mathrm{d}\lambda}$ and $J = r^2\frac{\mathrm{d}\theta}{\mathrm{d}\lambda}$ energy and angular momentum of emitted particle, respectively. Let us assume an emitted particle coming from just outside the BH horizon, the observer on the AdS boundary cannot detect this particle if there is a turning point that satisfies

$$\left(\frac{\mathrm{d}r}{\mathrm{d}\lambda}\right)^2 = 0.$$

An impact parameter is defined $b \equiv J/E$ and massless particle can reach infinity only if

$$\frac{1}{b^2} > \frac{f(r)}{r^2}, \tag{18}$$

$\forall\, r > r_+$. The impact parameter b_c is determined by maximum value of $f(r)/r^2$. It is useful in calculating evaporation process through the application of the Stefan–Boltzmann law [30, 60, 61]

$$\frac{\mathrm{d}M}{\mathrm{d}t} = -Cb_\mathrm{c}^2 T^4, \tag{19}$$

where the constant C is assumed to be unity for sake of simplicity. T is temperature, particularly the asymptotic plays a dominant role in the BH evaporation as the photon energy term T^4 possesses a higher order. To determine the photon sphere radius r_p and the

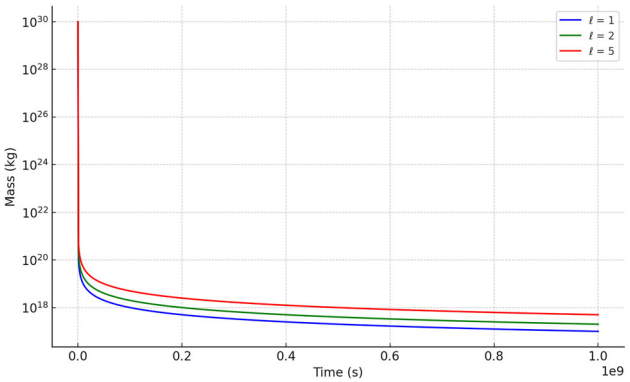

Fig. 1 Plot of mass of Bardeen BH ($c = 0$) versus t for various values of l with fixed $q = 0.4$ and $\omega = \frac{-2}{3}$

associated critical impact parameter b_c for the Bardeen–Kiselev black hole with a cosmological constant, we employ the standard method used for analyzing null geodesics in static, spherically symmetric spacetimes. The photon sphere corresponds to the location where massless particles can follow unstable circular trajectories under the black hole's gravitational influence. The critical impact parameter b_c, defined as the ratio of angular momentum to energy for such photon trajectories, marks the boundary separating photon paths that are captured by the black hole from those that escape to infinity. For a metric of the form considered here, the radius of the photon sphere is obtained by solving the extremum condition for the effective potential of null geodesics, leading to the following equation

$$\frac{\mathrm{d}}{\mathrm{d}r}\left(\frac{f(r)}{r^2}\right)\Big|_{r=r_\mathrm{p}} = 0,$$

where $f(r)$ denotes the metric function of the black hole spacetime. This condition isolates the stationary points of the effective potential experienced by photons, thereby determining the location of the unstable circular orbit. In the case of null geodesics, the effective potential governing photon motion is given by $f(r)/r^2$. Hence, to obtain the photon sphere radius, one differentiates this effective potential with respect to r and sets the resulting expression equal to zero. The requirement

$$\frac{\mathrm{d}}{\mathrm{d}r}\left(\frac{f(r)}{r^2}\right) = 0$$

therefore yields the radial position of the photon orbit in terms of the underlying metric function. Taking the derivative of the effective potential, we obtain

$$\frac{\mathrm{d}}{\mathrm{d}r}\left(\frac{f(r)}{r^2}\right) = \frac{f'(r)r^2 - 2rf(r)}{r^4}.$$

Setting this to zero gives the photon orbit condition

$$f'(r)r = 2f(r).$$

By inserting the explicit metric function $f(r)$ into the above condition, one can determine the value of r_p, which corresponds to the radius of the circular photon orbit. After obtaining r_p, the critical impact parameter b_c associated with massless particles follows directly from the relation

$$b_c = \frac{r_\mathrm{p}}{\sqrt{f(r_\mathrm{p})}}.$$

This relation provides the critical impact parameter at the photon sphere, distinguishing photon trajectories that spiral into the black hole from those that escape to spatial infinity. Using this result, and substituting the relevant quantities into the Stefan–Boltzmann law, we can compute

$$\mathrm{d}t = \ell^4 H_1(x, y)\mathrm{d}x. \tag{20}$$

Here, $H_1(x, y)$ represents a complex function that is too cumbersome to write. Solving this equation we determine the BH's lifetime

The behavior of BH mass with respect to time during the Hawking evaporation process is depicted in Figs. 1, 2, 3, and 4 for the Bardeen–AdS BH (i.e., with $c = 0$) under various values of the AdS curvature scale l and magnetic charge q, with a fixed equation of state parameter $\omega = -\frac{2}{3}$. In Fig. 1, the mass evolution is shown for $q = 0.4$, revealing that the BH mass decreases over time and approaches a finite value rather than vanishing completely. As l increases, the rate of evaporation becomes slower, and the remnant mass increases, indicating the strong influence of AdS curvature on BH evaporation. Figure 2 provides a density plot that numerically confirms this behavior, showing the terminal mass values as stable endpoints, which supports the notion of BH remnant formation due to the regularizing effects of nonlinear electrodynamics. Figures 3 and 4 further explore this dependence by

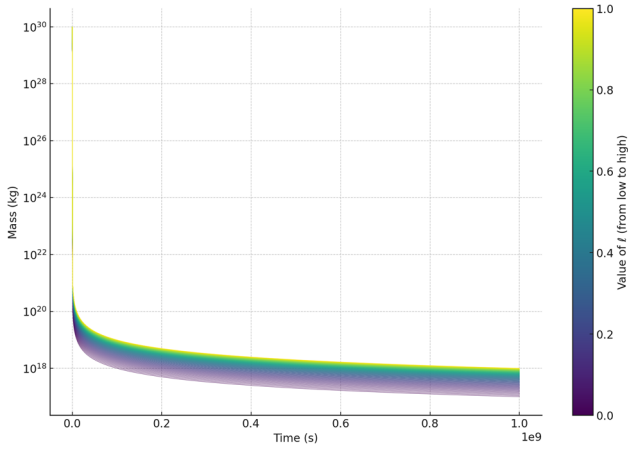

Fig. 2 Density plot for numerical results of Bardeen AdS black hole. The values of constant are same as in Fig. 1

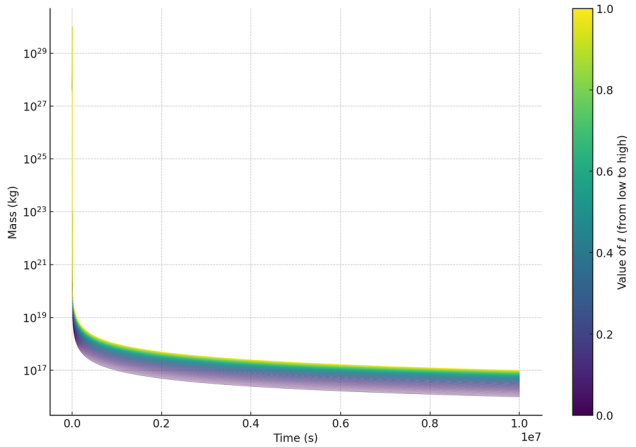

Fig. 3 Plot of mass of Bardeen BH ($c = 0$) versus t for various values of l with fixed $q = 0.3$ and $\omega = \frac{-2}{3}$

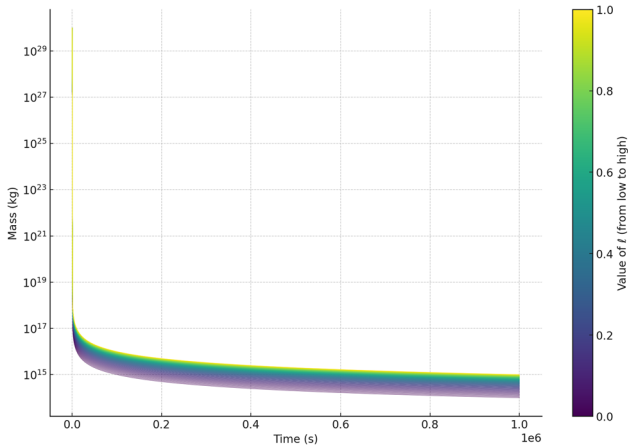

Fig. 4 Plot of mass of Bardeen BH ($c = 0$) versus t for various values of l with fixed $q = 0.2$ and $\omega = \frac{-2}{3}$

varying q; specifically, they show the mass evolution for $q = 0.3$ and $q = 0.2$, respectively. It is evident from the comparison that decreasing the magnetic charge accelerates the evaporation rate and reduces the remnant mass, which implies that magnetic charge plays a critical role in stabilizing the BH against complete evaporation. Mathematically, this behavior stems from the presence of the q-dependent term in the metric function $f(r)$, which modifies the spacetime geometry and hence the photon sphere and critical impact parameter. These alterations directly affect the Stefan–Boltzmann law-driven mass-loss rate. Physically, the presence of a magnetic monopole prevents total mass loss by introducing a repulsive core that halts further shrinkage, leading to the formation of a stable remnant. This is a remarkable deviation from the standard Schwarzschild or Kiselev–AdS cases, where complete evaporation is observed. Thus, the figures collectively highlight how nonlinear electrodynamics and magnetic charge result in profound physical modifications of the BH s long-term evolution and may offer a possible resolution to the information loss paradox through remnant preservation.

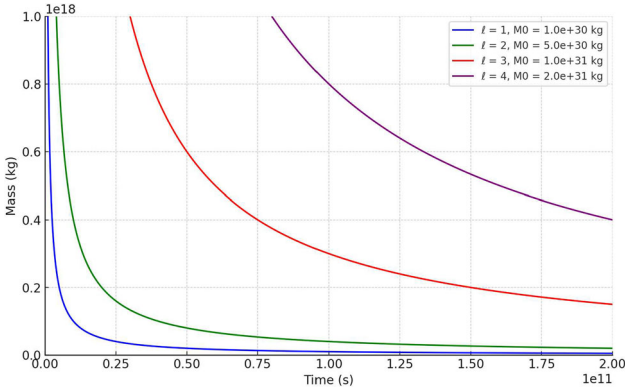

Fig. 5 Plot of mass of Kiselev BH ($q = 0$) versus t for various values of l and fixed $c = 0.4$ and $\omega = \frac{-2}{3}$

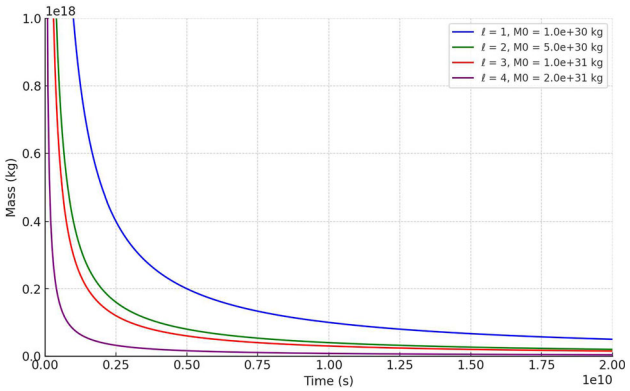

Fig. 6 Plot of mass of Kiselev BH ($q = 0$) versus t for various values of l and fixed $c = 0.2$ and $\omega = \frac{-2}{3}$

Figures 5 and 6 present the time evolution of the BH mass for the Kiselev–AdS BH, which corresponds to the special case where the magnetic charge $q = 0$, and hence no regularizing effects from nonlinear electrodynamics are present. In Fig. 5, the evaporation profiles are shown for a fixed quintessence normalization parameter $c = 0.4$ and various values of the AdS curvature parameter l, while Fig. 6 explores a similar setup for $c = 0.2$. Unlike the Bardeen–AdS case depicted in earlier figures, here the mass monotonically decreases and approaches zero in finite time, indicating a complete evaporation process without any remnant formation. The decrease in quintessence parameter c leads to a slower evaporation rate, showing that dark energy plays a significant role in modulating the Hawking radiation process. Additionally, the presence of a larger AdS radius (i.e., higher l) delays the evaporation, reflecting the influence of asymptotic spacetime curvature on energy loss mechanisms. These findings are consistent with the application of the Stefan–Boltzmann law, which incorporates the effective temperature T and critical impact parameter b_c, both of which are functions of the background geometry determined by $f(r)$. The absence of magnetic charge means the central singularity is not regularized; and thus, there is no repulsive core to halt the mass loss, resulting in the BH fully evaporating. Physically, this implies that in the absence of nonlinear electrodynamic corrections, the quintessence field alone cannot prevent the BH from vanishing, highlighting a stark contrast with the Bardeen case where magnetic charge-induced repulsion enables remnant formation. These comparative results demonstrate the crucial role of magnetic charge in altering the long-term fate of BHs and emphasize how distinct matter sources quintessence versus nonlinear electrodynamics affect BH thermodynamics and evolution.

4 Evolution of scalar perturbations of Bardeen–Kiselev black hole

The Klein–Gordon equation is a fundamental tool in quantum field theory in curved spacetime, that explains how scalar particles behave near strong gravitational fields. It connects BH physics with broader efforts in quantum gravity and semiclassical gravity. Scalar field perturbations governed by the Klein–Gordon equation provide a powerful framework to test BH stability, extract observable signatures, and explore the interplay between matter content and spacetime geometry in both classical and quantum regimes. The evolution of scalar perturbations helps us to determine whether a BH spacetime is stable or unstable under small disturbances. If perturbations decay over time, the BH is stable and if they grow, the spacetime may develop instabilities. In this section, we examine scalar perturbations that satisfy Klein–Gordon equation as [62]

$$\frac{1}{\sqrt{-g}}\partial_\mu\left(\sqrt{-g}g^{\mu\nu}\partial_\nu\Phi\right) = 0. \tag{21}$$

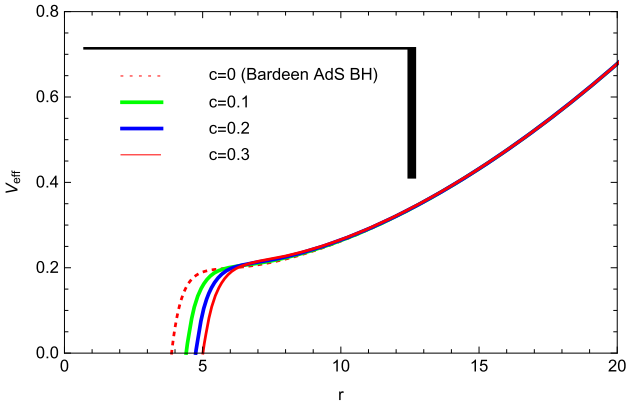

Fig. 7 Behavior of effective potential V_{eff} versus r for Bardeen–Kiselev AdS BH for various values of c with fixed $q = 0.2$ and $\omega = \frac{-2}{3}$

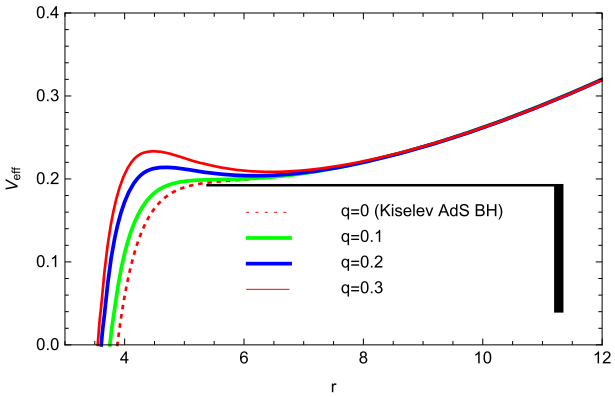

Fig. 8 Behavior of effective potential V_{eff} versus r for Bardeen–Kiselev AdS BH for various values of q with fixed $c = 0.2$ and $\omega = \frac{-2}{3}$

Here, scalar field is $\Phi = \Phi(t, r, \theta, \phi)$. By decomposing this field using spherical harmonics $Y_{lm}(\theta, \phi)$ as $\Phi = Y_{lm}\frac{\Psi(t,r)}{r}$, the equation for Ψ is derived as follows

$$\frac{\partial^2}{\partial x^2}\Psi + \left[-\frac{\partial^2}{\partial t^2} + V_{\text{eff}}(r)\right]\Psi = 0, \tag{22}$$

here effective potential V_{eff} is defined as

$$V_{\text{eff}} \equiv \frac{l(l+1)f(r)}{r^2} + \frac{1}{2r}\frac{\mathrm{d}(f(r)^2)}{\mathrm{d}r}, \tag{23}$$

with x being the coordinate defined as

$$\mathrm{d}r = f(r)\mathrm{d}x. \tag{24}$$

As r is dimensionless, x is dimensionless as well. Also it worth mentioning that spherical symmetry of the background makes the perturbations free for the choice of index m [44]. Thus, setting $m = 0$ retains the generality.

Figures 7 and 8 illustrate the behavior of the effective potential V_{eff} for scalar perturbations in the spacetime of Bardeen–Kiselev AdS BHs. These plots provide critical insight into the stability and wave dynamics around such BHs. In Fig. 7, the potential V_{eff} is plotted against the radial coordinate r for fixed magnetic charge $q = 0.2$ and varying values of the quintessence parameter c. The curves indicate that increasing c reduces the peak height of the potential barrier, implying a shallower well in which perturbations evolve. This decrease in the potential barrier suggests that scalar waves encounter less resistance when propagating through the spacetime, potentially increasing the transmission of radiation and lowering the trapping of modes, thereby modifying quasinormal mode frequencies. In contrast, Fig. 8 examines the variation of V_{eff} for fixed $c = 0.2$ while varying the magnetic charge q. It is observed that increasing q elevates the potential barrier significantly. This outcome reflects the fact that a stronger magnetic monopole structure, arising from nonlinear electrodynamics, enhances the repulsive core near the center, stabilizing the perturbations by creating a steeper effective potential. Mathematically, these behaviors stem from the form of the potential $V_{\text{eff}} = l(l+1)f(r)/r^2 + \frac{1}{2r}\frac{\mathrm{d}(f(r)^2)}{\mathrm{d}r}$, where $f(r)$ is influenced by both c and q. Physically, a higher q enhances the gravitational repulsion at small r, while a higher c representing dark energy exerts a diluting effect that reduces the confinement of perturbations. These competing influences directly affect the stability of the spacetime, gravitational wave damping times, and the energy distribution of scalar fields, thus providing distinct observational signatures for each parameter regime. The figures thereby highlight how magnetic charge and quintessence field distinctly modulate the dynamics of perturbations and contribute to the physical characteristics of BH spacetimes.

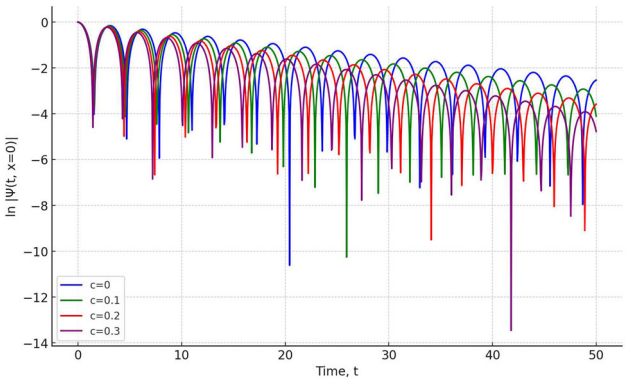

Fig. 9 Graph of $\ln|\Psi(t,\ x=0)|$ against t for Bardeen–Kiselev AdS BH. We use different values of c including $c=0$ for Bardeen AdS with fixed value $q=0.2$ and $\omega=\frac{-2}{3}$

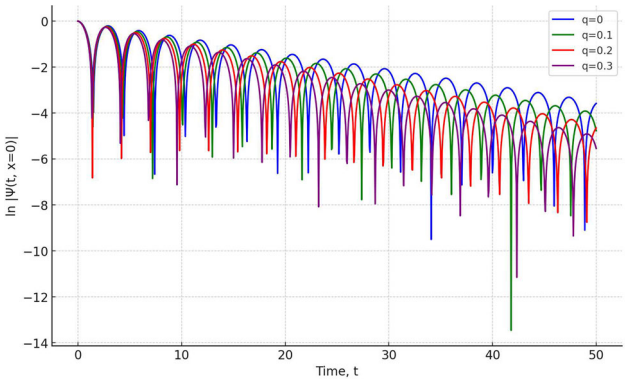

Fig. 10 Graph of $\ln|\Psi(t,\ x=0)|$ against t for Bardeen–Kiselev AdS BH. We use different values of q including $q=0$ for Kiselev AdS with fixed value of $c=0.2$ and $\omega=\frac{-2}{3}$

Firstly, we attempt to evaluate Eq. (22) in time scale using method given in Refs. [63–65].

Figures 9 and 10 present the time evolution of the scalar field perturbations for Bardeen–Kiselev AdS BHs by plotting $\ln|\Psi(t,\ x=0)|$ versus time t, thereby illustrating how the scalar wave decays in the vicinity of the BH. In Fig. 9, the decay of the perturbation field is shown for various values of the quintessence parameter c, with fixed magnetic charge $q=0.2$ and equation of state parameter $\omega=-\frac{2}{3}$. The curves demonstrate that increasing c results in faster decay rates and lower oscillation amplitudes, indicating that the presence of a stronger quintessence field enhances the damping of scalar perturbations. This behavior reflects a more dissipative geometry where dark energy drives the rapid attenuation of field disturbances. On the other hand, Fig. 10 shows the time evolution of the perturbation for varying values of magnetic charge q, with fixed $c=0.2$. It is evident that increasing q leads to a slower decay of the scalar field and increased oscillatory behavior. This can be attributed to the fact that the magnetic charge introduces a repulsive core via nonlinear electrodynamics, effectively increasing the depth and width of the effective potential well in which the perturbations evolve. Mathematically, the behavior of $\Psi(t,\ x=0)$ follows from solving the Klein–Gordon equation in a curved background, where the potential V_{eff} directly depends on both q and c. Physically, these findings suggest that quintessence contributes to faster energy dissipation from the BH, whereas magnetic charge tends to trap energy longer near the horizon, possibly stabilizing perturbations. The contrasting decay profiles provide key insights into the quasinormal mode structure and signal observable differences in gravitational wave emission, with potential applications in testing the presence of dark energy and regularizing magnetic fields in astrophysical BHs.

5 Greybody factors onto Bardeen–Kiselev AdS black hole

Hawking radiation is theoretically predicted to be emitted from BHs as a blackbody spectrum. However, this radiation has to pass through the curved spacetime around the BH before reaching an observer at infinity. During this journey, a fraction of the radiation is absorbed, scattered, or partially reflected by the gravitational potential surrounding BH. The greybody factor measures the portion of Hawking radiation that successfully escapes the black hole's gravitational barrier and reaches a distant observer. It therefore plays a key role in determining the observable spectrum of emitted particles, as it modifies the pure thermal radiation predicted at the event horizon into the spectrum detected at infinity. In their absence, the emission would resemble a perfect blackbody. Greybody factors carry essential information about the physical characteristics of a black hole, including its mass, charge, rotation, and the structure of the surrounding spacetime. By studying these factors, one can indirectly extract details about the underlying geometry and the nature of the compact object. Since greybody factors modify the intensity of Hawking radiation, they also play a significant role in determining the rate at which a black hole loses mass and energy, which is particularly important for understanding the

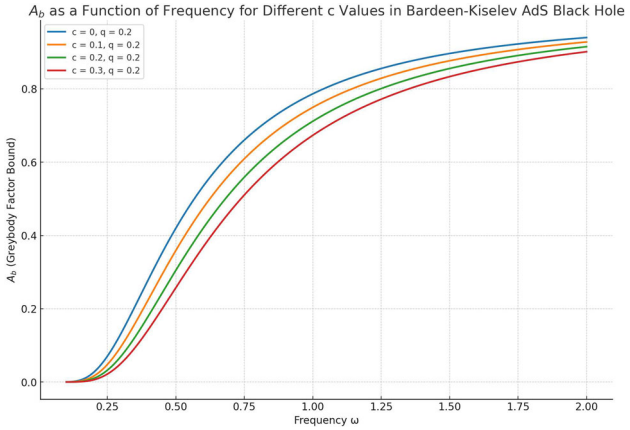

Fig. 11 Graph of A_b against frequency for Bardeen–Kiselev AdS BH. We use different values of c and fixed $q = 0.2$

evaporation process of small black holes. Various analytical and numerical techniques have been developed to evaluate greybody factors [66–70]. In the present work, we utilize rigorous bounds on greybody factors, which provide theoretical limits on the fraction of Hawking radiation that can escape the gravitational potential barrier. These bounds offer constraints on the relative portions of radiation that are transmitted, reflected, or absorbed, thereby yielding insight into the interaction between emitted particles and the black hole geometry. The bounds are sensitive to the black hole s parameters and the energy of the emitted quanta, making them powerful tools for probing black hole thermodynamics and radiation properties.

A systematic framework for establishing rigorous bounds on greybody factors was first put forward by Visser [71] and later extended by Boonserm and Visser [72]. Since then, this approach has been refined and applied in several subsequent works, including Refs. [73–78], where the method was generalized to various black hole spacetimes and field dynamics. In the present study, our focus is on the greybody factors associated with the Bardeen–Kiselev black hole geometry. To this end, we examine the propagation of a scalar field governed by the Klein–Gordon equation and analyze the corresponding effective potential, which is

$$V(r) = l(l+1)f(r)r^{-2} + f(r)f'(r)r^{-1}. \tag{25}$$

Using effective potential, we proceed to analyze bounds for Bardeen–Kiselev BHs by focusing on the influence of c and q. The expression for calculating the bound is presented as [79, 80]

$$A_b \geq \operatorname{sech}^2\left(\frac{1}{2\omega}\int_{-\infty}^{\infty}\frac{|V|}{f(r)}\mathrm{d}r\right), \tag{26}$$

It is worth noting that $A_b = T_b$ [81]. The modified boundary conditions are described as follows

$$A \geq A_b = \operatorname{sech}^2\left(\frac{A_l}{2\omega}\right). \tag{27}$$

with

$$A_l = \int_{r_H}^{R_H}\frac{|V|}{f(r)}\mathrm{d}r = \int_{r_H}^{R_H}\left|\frac{l(l+1)}{r^2} + \frac{f'(r)}{r}\right|\mathrm{d}r. \tag{28}$$

Here, A_b and T_b represent the absorption and transmission coefficients associated with the near horizon region, while A and A_l denote the corresponding coefficients defined at large r. The subscripts b and l refer to the BH horizon and the asymptotic (cosmological) boundary, respectively. Thus, we have effectively calculated rigorous bounds on GFs for Bardeen–Kiselev BHs as a function of various parameters, such as c and q. Through numerical computations, we can assess the bound and represent it visually.

Figures 11, 12, 13, 14, and 15 illustrate the behavior of the GF bounds $\mathcal{A}_b$ for Bardeen–Kiselev AdS BHs, as a function of frequency ω, under various values of the quintessence parameter c and magnetic charge q. These bounds are derived using a rigorous analytical method based on the integral of the effective potential $V(r)$, as given by $\mathcal{A}_b \geq \operatorname{sech}^2\left(\frac{1}{2\omega}\int_{-\infty}^{\infty}\frac{|V(r)|}{f(r)}\mathrm{d}r\right)$, which quantifies the minimal transmission probability for scalar particles radiated via Hawking processes. In Figs. 11 and 12, the variation of $\mathcal{A}_b$ with increasing c for fixed $q = 0.2$ shows that larger quintessence values lower the greybody bound across all frequencies, indicating enhanced suppression of Hawking radiation due to the repulsive influence of the surrounding dark energy field. This is corroborated in the density plot (Fig. 12), which visually highlights how the transmission probability diminishes as c increases. In contrast, Figs. 13 and 14 examine the variation of $\mathcal{A}_b$ for different values of magnetic charge q while fixing $c = 0.2$. The plots reveal that increasing q significantly boosts the GF, especially at lower frequencies, implying that the magnetic field structure introduced via nonlinear electrodynamics enhances the probability of particle emission. These trends are further reinforced in Fig. 15, where the combined effects of c and q are shown; a strong magnetic charge tends to counteract the suppressive influence of quintessence, leading to a more balanced radiation spectrum. Physically, this analysis demonstrates that the GFs, and hence the emitted radiation spectrum, are highly

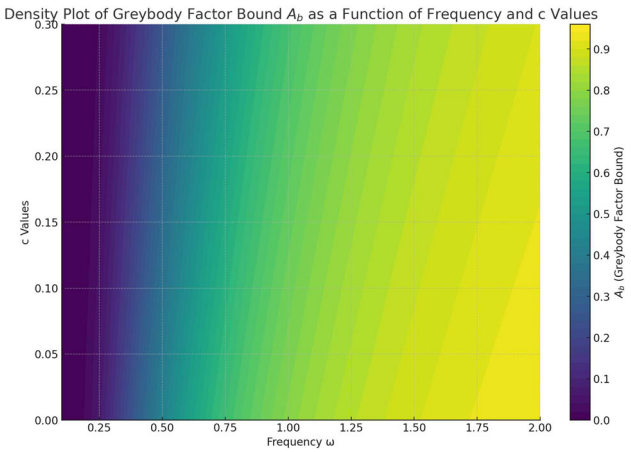

Fig. 12 Density plot of A_b versus frequency for Bardeen–Kiselev AdS BH. We use different values of c and fixed $q = 0.2$

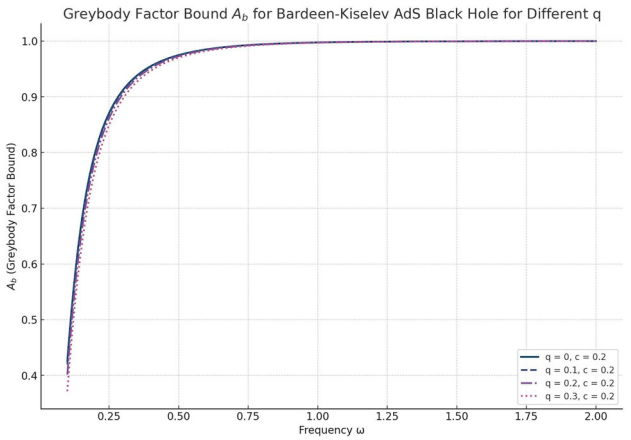

Fig. 13 Plot of A_b as a function of the frequency for Bardeen–Kiselev AdS BH. We use different values of q and fixed $c = 0.2$

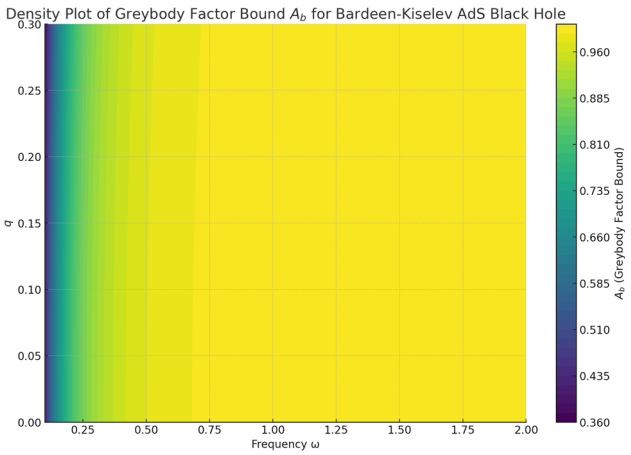

Fig. 14 Density plot of A_b versus frequency for Bardeen–Kiselev AdS BH. We use different values of q and fixed $c = 0.2$

sensitive to the surrounding matter content and field configurations. The quintessence field acts to trap radiation more effectively, whereas magnetic charge facilitates its escape. These effects directly influence the rate of mass loss and the thermodynamic stability of the BH. The results underscore the importance of including both nonlinear electrodynamic and dark energy components when modeling realistic BH evaporation scenarios in modified gravity or AdS/CFT frameworks.

6 Shadows of Bardeen–Kiselev black hole

The shadow of a BH is the dark region observed against a background of light when light rays emitted by surrounding material (like an accretion disk) are bent, absorbed, or captured by the BH's intense gravitational field. It is not the event horizon itself, but a 2D

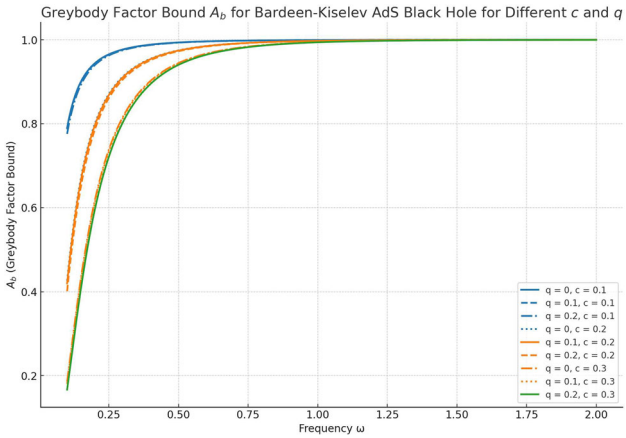

Fig. 15 Plot of A_b versus frequency for Bardeen–Kiselev AdS BH. We use different values of q and c

projection of the photon sphere the region where photons move in unstable circular orbits. Light rays that come close to the black hole can escape to infinity (contributing to the visible ring), be captured by the BH (contributing to the dark interior), Or orbit for a while before escaping, leading to secondary images. This complex lensing effect forms a luminous ring called the photon ring surrounding the central dark region, which is the BH shadow. The size and shape of shadow depend on BH s spacetime geometry, spin, and surrounding matter distribution.

In this analysis, we start from the Lagrangian of the form [82]

$$L = \frac{1}{2} g_{\mu\nu} \dot{x}^{\mu} \dot{x}^{\nu} = \frac{1}{2}\left(\frac{1}{f(r)} \dot{r}^2 + r^2 \sin^2\theta \dot{\phi}^2 - f(r)\dot{t}^2 + r^2 \dot{\theta}^2 \right), \tag{29}$$

where a dot denotes differentiation with respect to the affine parameter τ. Applying the Euler–Lagrange equations to this Lagrangian, one can readily obtain the equations of motion, yielding [82]

$$E = \left(1 - \frac{2m}{r} + \frac{d_1 \kappa_s^2 - 4 e_1 \kappa_d^2 - 2 f_1 \kappa_{sh}^2}{r^2} \right) \dot{t}, \tag{30}$$

$$P_{\phi} = r^2 \sin^2\theta \dot{\phi} = L. \tag{31}$$

Here, energy is E and angular momentum is L of particle. The next step is to determine the particle trajectory by solving the corresponding geodesic equations, which can be obtained using the Hamiltonian formalism [82].

$$H + \frac{\partial S}{\partial \tau} = 0, \tag{32}$$

$$H = \frac{1}{2} g_{\mu\nu} p^{\mu} p^{\nu}. \tag{33}$$

Using the relation $\frac{\partial S}{\partial x^{\mu}} = p^{\mu}$ together with the separation of variables technique originally introduced by Carter [82],

$$S = \frac{\tilde{m}^2}{2}\tau - Et + S_{\theta}(\theta) + L\phi + S_r(r), \tag{34}$$

we derive the following important relation

$$\frac{E^2}{f(r)} - \frac{1}{r^2}\left(\frac{L^2}{\sin^2\theta} + K - L^2 \cot^2\theta \right) - f(r)\left(\frac{\partial S_r}{\partial r} \right)^2 - \frac{1}{r^2}\left(\frac{\partial S_{\theta}}{\partial \theta} \right)^2 + L^2 \cot^2\theta - K = 0. \tag{35}$$

Here, K denotes the Carter separation constant. Since we are dealing with photon trajectories, the particle mass must be set to zero, i.e., $\tilde{m} = 0$, consistent with the null geodesic condition. Using this constraint, the equations simplify appropriately for the massless case. $\frac{\partial S_{\theta}}{\partial \theta} = p_{\theta}$, and $\frac{\partial S_r}{\partial r} = p_r$, one can easily obtain the following

$$\frac{\partial S_{\theta}}{\partial \theta} = r^2 \frac{\partial \theta}{\partial \tau}, \tag{36}$$

$$\frac{\partial S_r}{\partial r} = f(r)^{-1} \frac{\partial r}{\partial \tau}. \tag{37}$$

Substituting Eqs. (36) and (37) into Eq. (35) allows us to reorganize the expression into two separate relations, each corresponding to different components of the motion. This separation facilitates a clearer analysis of the radial and angular dynamics of the photon trajectory.

$$r^2\left(\frac{\partial S_r}{\partial r}\right)^2 = r^2E^2 f(r)^{-2} - (L^2+K)f(r)^{-1}, \tag{38}$$

$$\left(\frac{\partial S_\theta}{\partial \theta}\right)^2 = -L^2\cot^2\theta + K. \tag{39}$$

Next, we utilize the definition of canonically conjugate momentum show complete set of equations

$$r^2\frac{\partial\theta}{\partial\tau} = \pm\sqrt{\Theta}, \quad \Theta = -L^2\cot^2\theta + K, \tag{40}$$

$$r^2\dot{r} = \pm\sqrt{R}, \quad R = r^4E^2 - (L^2+K)r^2 f(r), \tag{41}$$

in which

$$\Theta = K - L^2\cot^2\theta, \tag{42}$$

and

$$R(r) = r^4E^2 - (L^2+K)r^2 f(r). \tag{43}$$

In these expressions, the symbols + and—correspond to radially outgoing and ingoing photon paths, respectively. The existence of unstable null trajectories determines the boundary of the black hole shadow. To proceed with computing these orbits, we express the geodesic equation in the form

$$V_{\text{eff}}(r) + \left(\frac{\partial r}{\partial\tau}\right)^2 = 0. \tag{44}$$

where the effective potential $V_{\text{eff}}(r)$ takes the form

$$V_{\text{eff}}(r) = f(r)\big(L^2+K\big)r^{-2} - E^2. \tag{45}$$

Figures 16 and 17 illustrate the shadow images of Bardeen–Kiselev AdS BHs, showing how the presence of quintessence and magnetic charge alters the silhouette observed by a distant observer. In Fig. 16, the shadow morphology is analyzed for increasing values of the quintessence parameter c while keeping the magnetic charge q fixed. The plots reveal that as c increases, the size of the shadow becomes smaller and more compressed, indicating a stronger influence of the repulsive dark energy field which modifies the null geodesics by pushing photon orbits outward and thereby shrinking the photon sphere. In contrast, Fig. 17 examines the effect of varying magnetic charge q with a fixed c and demonstrates that larger values of q lead to an expanded shadow size. This is due to the magnetic monopole structure from nonlinear electrodynamics which introduces an effective repulsion near the BH core, stabilizing photon orbits at larger radii and enlarging the boundary of the photon sphere. These results are obtained by analyzing the geodesic equations derived from the Hamilton–Jacobi formalism, in which the shadow boundary is determined by the unstable circular photon orbits where the effective potential satisfies the condition $V_{\text{eff}}(r) + (\partial r/\partial\tau)^2 = 0$. The mathematical relation for the shadow radius involves the critical impact parameter $b = r_{\text{p}}/\sqrt{f(r_{\text{p}})}$, where r_{p} is the photon orbit radius, itself sensitive to changes in c and q via the metric function $f(r)$. Physically, these figures show how the presence of dark energy (through c) tends to suppress the apparent size of the BH, while the magnetic field (through q) counteracts this compression and restores or enlarges the observable shadow. The interplay between these parameters offers unique signatures that could, in principle, be identified through precise observations such as those from the Event Horizon Telescope. These findings provide valuable insights into the nature of regular BHs in AdS spacetimes, and illustrate how their optical appearances encode information about the underlying matter and field content.

7 Analysis of the accretion disk around Bardeen–Kiselev AdS

The Novikov Thorne model is a theoretical framework that describes the structure and emission properties of geometrically thin, optically thick accretion disks around BHs. It extends the earlier Newtonian model by Shakura and Sunyaev (1973) into general relativistic settings, making it applicable to strong gravitational fields near BHs. It provides a realistic model for the thermal emission from accretion disks. The model is used to fit X-ray spectra from accreting BHs, helping to estimate BH spin, mass and infer accretion rates and disk properties. In shadow and image modeling (like in the Event Horizon Telescope), the Novikov–Thorne disk is often assumed as the emission source. It helps in understanding brightness asymmetries, secondary images, and photon ring structures. A comprehensive description of the Novikov–Thorne thin accretion disk formalism is provided in Ref. [83]. For a distant observer, the cumulative bending of photon trajectories, which governs the resulting image structure, can be written as [84]

$$\psi(u) = \int_{u_{\text{source}}}^{u_{\text{obs}}} \frac{1}{\Omega(u)}\mathrm{d}u = \int_{u_{\text{source}}}^{u_{\text{obs}}} \left(\frac{1}{b^2} - u^2 f(u)\right)^{-1/2}\mathrm{d}u, \tag{46}$$

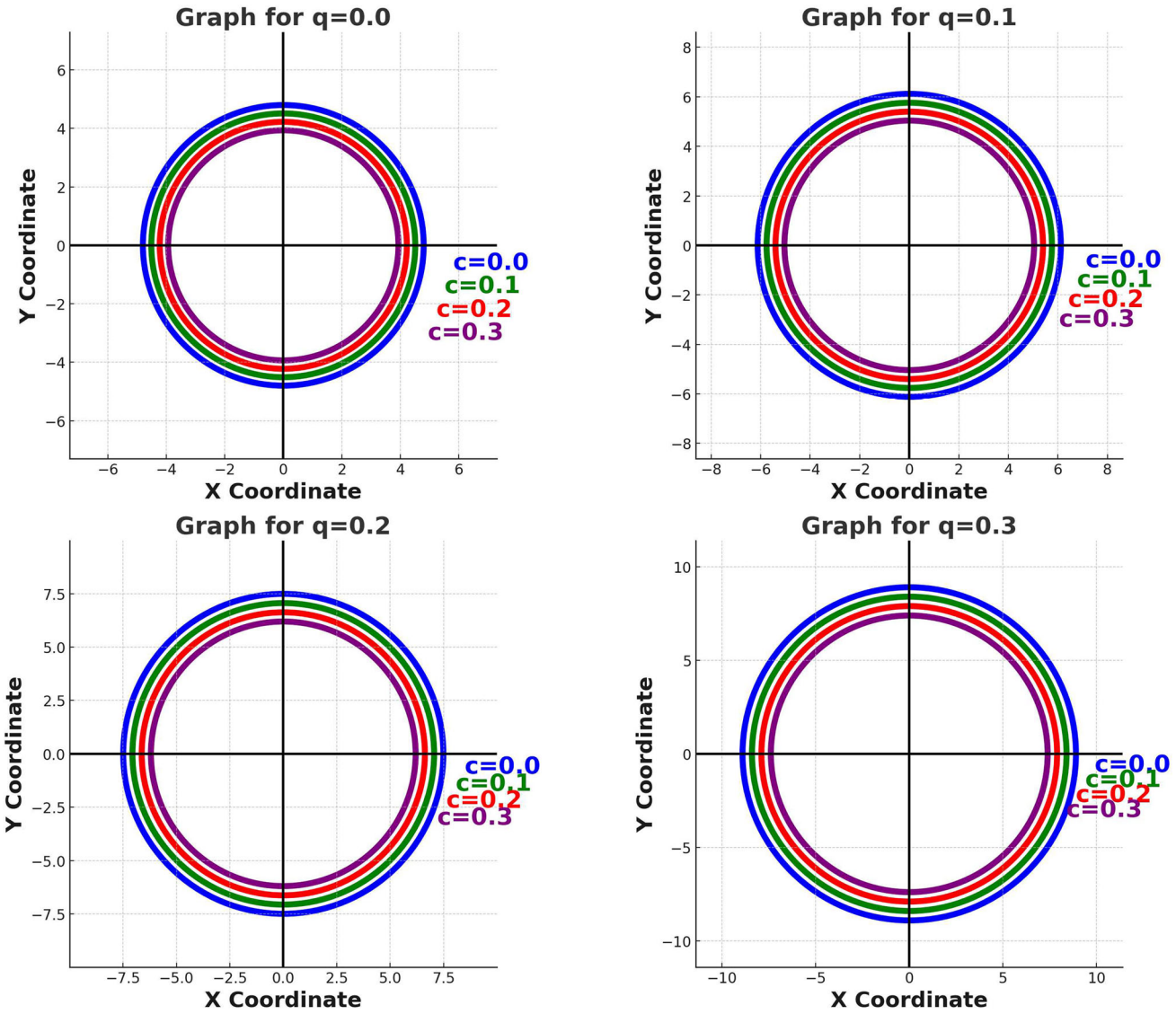

Fig. 16 Plot of shadows of Bardeen–Kiselev AdS BH for different values of quintessence and magnetic charge

Here, we introduce the substitution $u = r^{-1}$. The quantity u_{source} refers to the inverse radial position of the emission point of the photon, whereas u_{obs} corresponds to the position of the observer. For certain values of the impact parameter exceeding a critical threshold, the photon trajectory may exhibit a turning point in the radial direction, denoted by u_0. In such cases, the photon path can be separated into two segments: one running from u_{source} to u_0, and the second from u_0 to u_{obs}. The turning point u_0 is determined through the condition

$$u_0 = \frac{1}{b^2} f(r)^{-1}, \tag{47}$$

In this part of the analysis, numerical integration techniques are employed to generate the primary and secondary images. The corresponding photon trajectories are computed using the following relation [84]

$$\int_{u_{\text{source}}}^{u_{\text{obs}}} \left(\frac{1}{b^2} - u^2 f(u)\right)^{-1/2} \mathrm{d}u = \pi n - \cos^{-1}\left(\frac{1}{\sqrt{\sin^2\eta \tan^2\theta + 1}} \tan\theta \sin\eta\right), \tag{48}$$

In this expression, η represents the celestial angle, b denotes the impact parameter, and θ corresponds to the observer's inclination angle. The integer n specifies the image order, where $n = 0$ refers to the direct image and $n = 1$ corresponds to the secondary lensed image. Thus, the path of each photon is characterized by its azimuthal angle η together with the associated impact parameter b, which jointly determine the apparent position of the image seen by the observer. From this expression, the observer's inclination

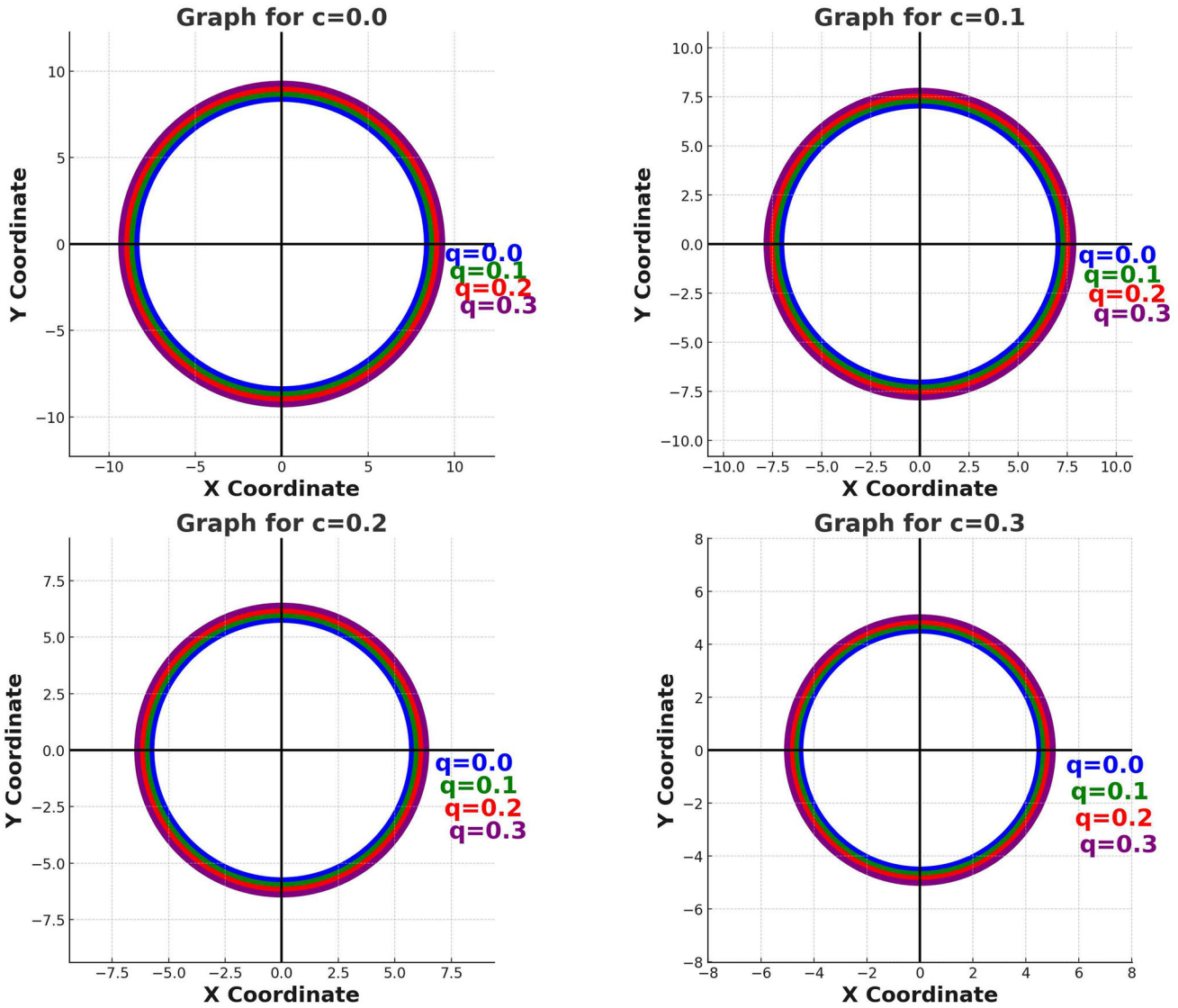

Fig. 17 Plot of shadows of Bardeen–Kiselev AdS BH for different values of quintessence and magnetic charge

angle can be directly inferred. For a fixed radial distance r, the relation can be rewritten to express the dependence between the impact parameter b and the polar angle η associated with a particular trajectory.

The spacetime parameters of the metric enter the equation as constants, allowing one to probe how variations in these parameters influence both the underlying geometry and the observable structure of the accretion disk. Since an explicit analytical integration for u is generally not feasible, one can restrict η to the interval $[0, \pi]$ and employ a numerical root-finding procedure to determine the corresponding value of b. This value of the impact parameter then maps directly to the apparent image of the orbit as seen by a distant observer.

Figures 18, 19 and 20 depict the optical appearances of thin accretion disks around the Bardeen–Kiselev AdS BH, highlighting how variations in the quintessence parameter c, magnetic charge q, and observer inclination angle θ alter the direct and secondary disk images. These simulations are based on the Novikov–Thorne model, which incorporates general relativistic effects on photon trajectories and is well-suited for modeling thin, optically thick disks in strong gravitational fields. In Fig. 18, the accretion disk images are shown for increasing values of c with fixed magnetic charge and observer angle. As c increases, both the direct and secondary images of the disk become increasingly distorted and compressed, particularly in the vertical direction, due to the enhanced repulsive effects of the surrounding quintessence field. This results in tighter bending of light rays and more extreme lensing near the horizon. In Fig. 19, the magnetic charge q is varied while holding c constant. It is observed that higher values of q lead to greater asymmetry and deformation in the disk structure, especially for the secondary images. This is attributed to the magnetic monopole effect, which modifies the photon sphere and enhances the radial distance at which null geodesics are deflected, thereby altering the brightness and shape of the lensed images. Finally, Fig. 20 investigates the impact of changing the observer inclination angle θ. As

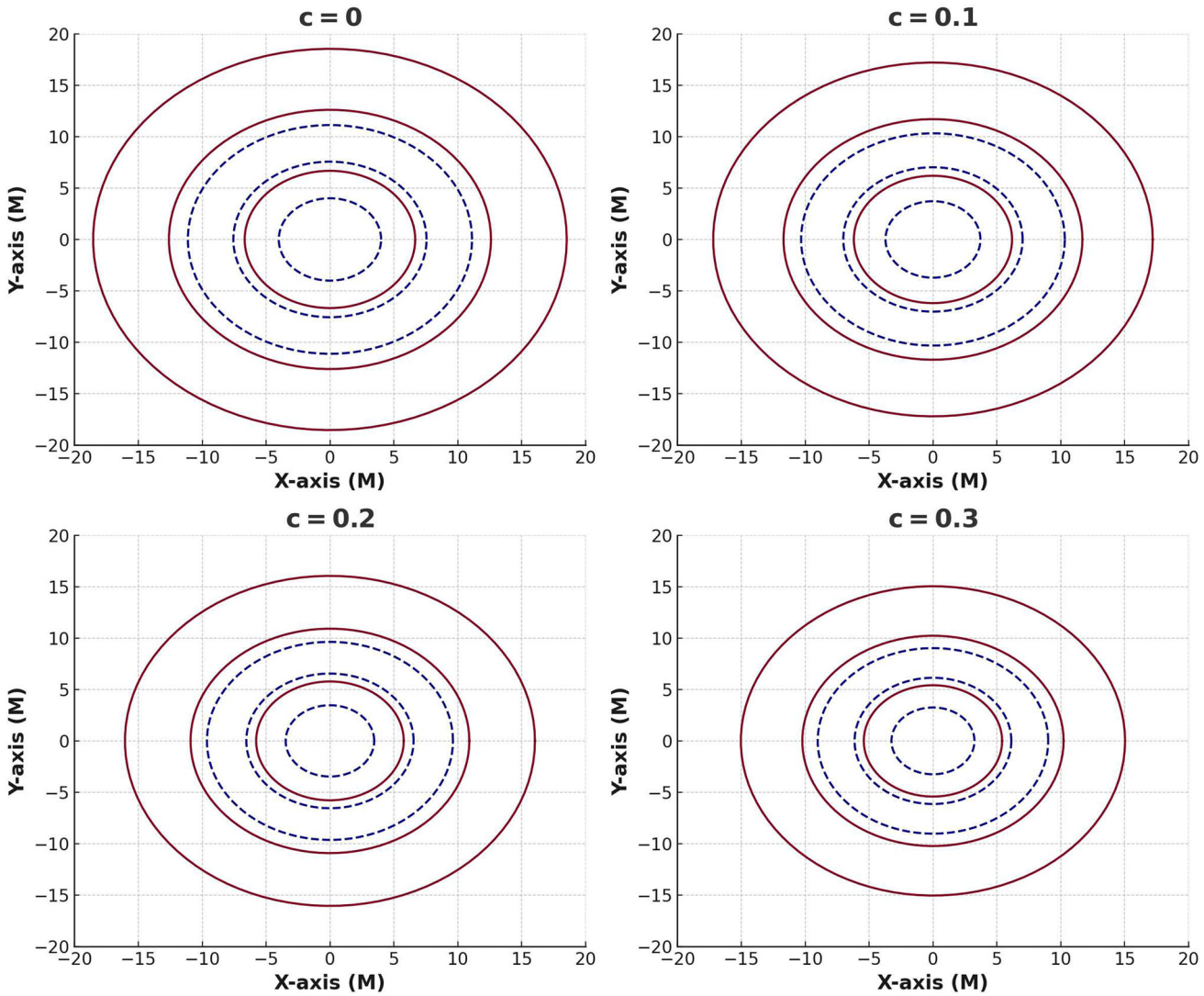

Fig. 18 Accretion disk around Bardeen–Kiselev BH for different values of $c = 0, 0.1, 0.2, 0.3$. Red and blue curves correspond to direct and secondary images, respectively, for different values of $r = 9, 17$ and 25

θ increases from a face-on to an edge-on view, the accretion disk appears more flattened and elongated, with the secondary images wrapping more tightly around the BH and exhibiting increased relativistic beaming. Mathematically, these image constructions are based on integrating the ray-tracing equation involving the impact parameter b and azimuthal angle η, with null geodesics governed by the effective potential $R(r) = r^4E^2 - (L^2 + K)r^2 f(r)$.

8 Conclusion

In this work, we have conducted a comprehensive and multifaceted investigation into the physical properties and observational signatures of the Bardeen–Kiselev BH in AdS spacetime. Motivated by the compelling need to resolve central singularities and account for dark energy effects within BH environments, we adopted a hybrid framework that unites nonlinear electrodynamics (via magnetic monopole charge) with quintessence fields, offering a more physically viable and regular BH solution. This model is particularly significant in the context of the AdS/CFT correspondence and modern observational advancements.

In the first stage of the analysis, we reviewed the geometric structure of the Bardeen–Kiselev–AdS BH and derived thermodynamic quantities such as the Hawking temperature and mass via the surface gravity and horizon radius. We demonstrated that the combination of magnetic charge and quintessence introduces a rich parameter space, wherein the thermodynamic behavior significantly deviates from traditional singular BH solutions. Our study of Hawking evaporation revealed that in the presence of magnetic charge ($q \neq 0$), the BH does not completely evaporate but stabilizes to a finite remnant mass, while in the pure Kiselev–AdS limit ($q = 0$), complete

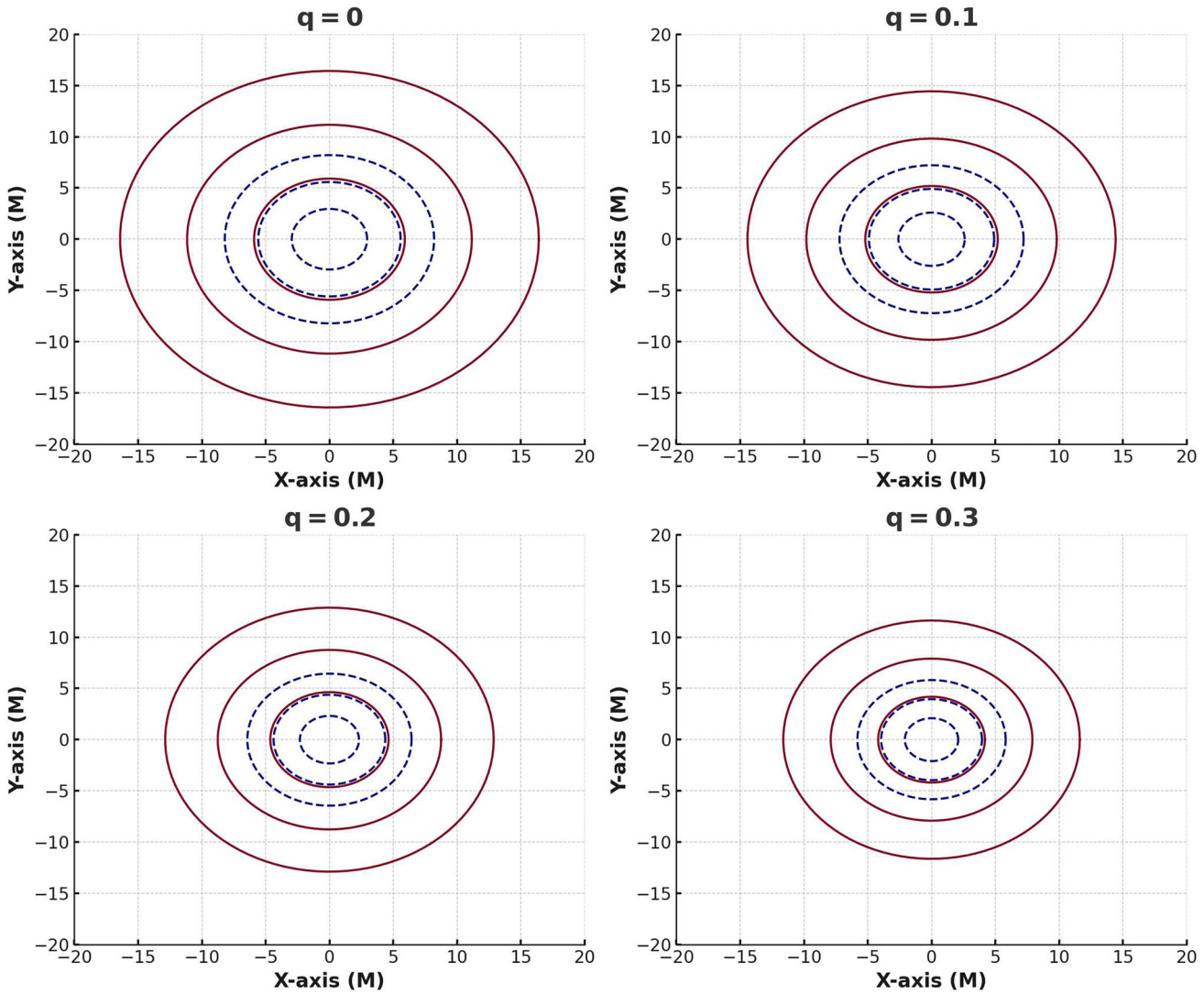

Fig. 19 Accretion disk around Bardeen–Kiselev BH for different values of $q = 0, 0.1, 0.2, 0.3$. Red and blue curves correspond to direct and secondary images, respectively, for different values of $r = 9, 17$ and 25

evaporation occurs. This finding provides crucial insight into the possible resolution of the information loss paradox via remnant formation. Next, the evolution of scalar perturbations was analyzed through the Klein–Gordon equation in curved spacetime. The effective potential and time-domain profiles showed that increasing the quintessence parameter c leads to faster damping of scalar waves, while higher magnetic charge q introduces stronger trapping potential, indicating enhanced stability. These results reinforce the idea that dark energy contributes to dissipative dynamics, whereas nonlinear electrodynamic corrections introduce repulsive cores that can stabilize the spacetime. In the context of Hawking radiation, we derived rigorous bounds on the GFs using the Visser–Boonserm formalism. We observed that increasing c suppresses the GF, reducing the radiation's escape probability, while larger q boosts the GF, enhancing emission. These findings emphasize the delicate balance between gravitational trapping due to quintessence and radiation leakage induced by magnetic charge, thereby controlling the BH's evaporation profile and energy loss rate.

Furthermore, we analyzed the shadow cast by the Bardeen–Kiselev–AdS BH using null geodesics and Hamilton–Jacobi methods. The results revealed that quintessence shrinks the apparent size of the shadow, while magnetic charge enlarges it. This interplay directly modifies the photon sphere and the critical impact parameter, establishing clear optical signatures that could potentially be detected by instruments like the Event Horizon Telescope. Finally, by employing the Novikov–Thorne thin accretion disk model, we simulated the images of the accretion disk for different values of c, q, and observer inclination angle θ. The direct and secondary images exhibited considerable changes in disk brightness, shape, and distortion, with higher c leading to more compact and compressed images, and increasing q introducing asymmetry and lensing enhancement. These optical deformations provide observational imprints of the underlying spacetime geometry and the surrounding matter-energy content.

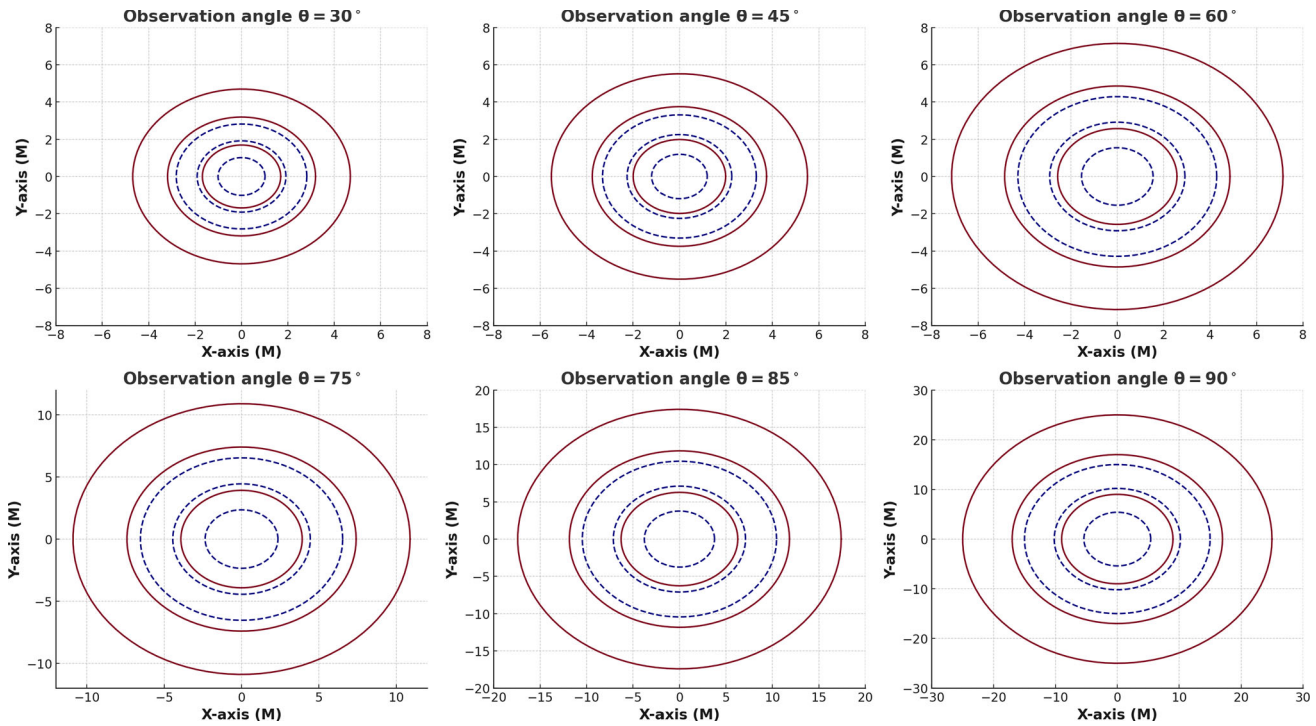

Fig. 20 Accretion disk around Bardeen–Kiselev BH for different values of observation angle. Red and blue curves correspond to direct and secondary images, respectively, for different values of $r = 9$, 17 and 25

In our analysis, we observe that the evaporation of the Bardeen–Kiselev BH does not proceed to completion. Instead, the Hawking temperature decreases to a minimum non-zero value as the horizon radius approaches a critical scale. This behavior leads to a halt in the evaporation process and results in the formation of a stable black hole remnant characterized by a finite mass and radius. Physically, this scenario arises due to the combined effects of nonlinear electrodynamics and the surrounding quintessence field, both of which modify the near horizon structure and regularize the geometry, preventing complete mass loss. Such remnants are of particular interest in discussions of the information paradox, as they may retain the quantum information encoded during the collapse and evolution of the BH. While a complete resolution of the paradox requires a fully quantum gravitational treatment, our results suggest that regular black hole remnants can serve as potential information carriers, avoiding the total destruction of information that would occur in complete evaporation models. Thus, the existence of long-lived remnants in this spacetime offers a viable and physically motivated mechanism that contributes to ongoing efforts toward understanding information recovery in black hole evaporation.

Acknowledgements The authors extend their appreciation to the Deanship of Research and Graduate Studies at King Khalid University for funding this work through Large Research Project under grant number RGP2/140/46.

Data Availability No data associated in the manuscript.

Declarations

Conflict of interest The authors declare that they have no Conflict of interest.

References

1. E. Berti et al., Class. Quant. Grav. **32**, 243001 (2015)
2. L. Barack et al., Class. Quant. Grav. **36**, 143001 (2019)
3. B.P. Abbott et al., Phys. Rev. X **9**, 031040 (2019)
4. R. Abbott et al., Astrophys. J. Lett. **896**, L44 (2020)
5. K. Akiyama et al., Astrophys. J. Lett. **875**, L5 (2019)
6. K. Akiyama et al., Astrophys. J. Lett. **875**, L6 (2019)
7. V. Cardoso, E. Franzin, P. Pani, Phys. Rev. Lett. **116**, 171101 (2016)
8. K.A. Bronnikov, A.M. Galiakhmetov, Phys. Rev. D **94**, 124006 (2016)
9. J.L. Blázquez-Salcedo, C. Knoll, E. Radu, Phys. Rev. Lett. **126**, 101102 (2021)

10. S.L. Liebling, C. Palenzuela, Living Rev. Rel. **15**, 6 (2012)
11. F.S.N. Lobo et al., Phys. Rev. D **103**, 084052 (2021)
12. E. Franzin et al., JCAP **07**, 036 (2021)
13. W. Berej et al., Gen. Rel. Grav. **38**(885), 906 (2006)
14. E.L.B. Junior, M.E. Rodrigues, M.V.S. Silva, Nucl. Phys. B **961**, 115244 (2020)
15. H. Huang, J. Yang, Phys. Rev. D **100**, 124063 (2019)
16. K.A. Bronnikov, S.G. Rubin, (World Scientific Singapore, 2013)
17. G. Feng, S. Yu, T. Wang, Z. Zhang, Ann. Phys. **473**, 169903 (2025)
18. J. M. Bardeen, in *Proceedings of the International Conference GR5, Tbilisi, U.S.S.R.* (1968)
19. E. Ayon-Beato, A. Garcia, Phys. Lett. B **493**, 149–152 (2000)
20. M. Huo, Z. Fan, J. Qi, N. Qi, D. Zhu, J. Guid. Control Dyn. **46**(5), 1015–1022 (2023)
21. H.C.D. Lima, L.C.B. Crispino, Int. J. Mod. Phys. D **29**, 2041014 (2020)
22. C. Qiao, X. Long, L. Yang, Y. Zhu, W. Cai, Astrophys. J. **991**(1), 46 (2025)
23. K.A. Bronnikov, V.N. Melnikov, H. Dehnen, Gen. Rel. Grav. **39**(973), 987 (2007)
24. T.Y. Zhou, Y. Xie, Eur. Phys. J. C **80**, 1070 (2020)
25. J. Xu, X. Jiang, Y. Wang, N. Dong, L. Qiao, J. Bai, Chin. J. Aeronaut. **2025**, 103688 (2025)
26. S.W. Hawking, Nature **248**, 30 (1974)
27. S.W. Hawking, Commun. Math. Phys. **43**, 199 (1975); Erratum: *Commun. Math. Phys.***46**, 206 (1976)
28. J. Deng, N. Gao, X. Chen, Thin-Walled Struct. **184**, 110459 (2023)
29. D.N. Page, Phys. Rev. D **13**, 198 (1976)
30. J. Deng, N. Gao, Int. J. Mech. Sci. **233**, 107641 (2022)
31. B.P. Abbott et al., Phys. Rev. X **9**, 031040 (2019)
32. Y. Gong, J. Luo, B. Wang, Nat. Astron. **5**(881), 889 (2021)
33. Cosmic Explorer Project, https://cosmicexplorer.org
34. ET Steering Committee Editorial Team, *ET Design Report Update 2020*, ET-0007A-20 (2020)
35. LISA Mission, https://www.lisamission.org
36. S. Liu, Y. Hu et al., Phys. Rev. D **101**, 103027 (2020)
37. W.-H. Ruan et al., Int. J. Mod. Phys. A **35**, 2050075 (2020)
38. S. Kawamura et al., arXiv:2006.13545 [gr-qc]
39. Y. Sekhmani et al., Eur. Phys. J. C **85**(3), 1–26 (2025)
40. B. Turimov, S. Usanov, Y. Khamroev, Phys. Dark Universe **48**, 101876 (2025)
41. C. Zhang, Y. Gong, D. Liang, B. Wang, JCAP **06**, 054 (2023)
42. S. Rakhmanov et al., Eur. Phys. J. B **98**(2), 35 (2025)
43. E.W. Leaver, Proc. R. Soc. Lond. A **402**, 285–298 (1985)
44. S. Chandrasekhar, (Oxford University Press, Oxford, 1992)
45. K.D. Kokkotas, B.G. Schmidt, Living Rev. Rel. **2**, 1 (1999)
46. J. Deng, N. Gao, X. Chen, H. Pu, J. Guo, Ocean Eng. **278**, 114376 (2023)
47. V. Akhmedova et al., Phys. Lett. B **666**, 269–271 (2008)
48. S. Fernando, Gen. Rel. Grav. **37**, 461–481 (2005)
49. M.E. Rodrigues, M.V.S. Silva, H.A. Vieira, Phys. Rev. D **105**, 084043 (2022)
50. K.A. Bronnikov, Phys. Rev. D **63**, 044005 (2001)
51. E. Ayon-Beato, A. Garcia, Phys. Rev. Lett. **80**(23), 5056 (1998)
52. V.V. Kiselev, Class. Quant. Gravity **20**(6), 1187 (2003)
53. A. Bokulic, I. Smolic, T. Juric, Phys. Rev. D **105**(2), 024067 (2022)
54. K.A. Bronnikov, Regular black holes sourced by nonlinear electrodynamics (2022). arXiv preprint arXiv:2211.00743
55. B. Malakolkalami, K. Ghaderi, Astrophys. Space Sci. **357**, 112 (2015)
56. R.M. Wald, Living Rev. Rel. **4**, 6 (2001)
57. S. Gunasekaran, R.B. Mann, D. Kubiznk, JHEP **11**, 110 (2012)
58. A. Bokulic, I. Smolic, T. Juric, Phys. Rev. D **103**(12), 124059 (2021)
59. J.D. Bekenstein, Phys. Rev. D **7**, 2333–2346 (1973)
60. P. Landsberg, A. De Vos, J. Phys. A: Math. Gen. **22**, 1073 (1989)
61. T.R. Cardoso, A.S. de Castro, Rev. Bras. Ens. Fis. **27**, 559 (2005)
62. R.G. Daghigh, M.D. Green, G. Kunstatte, Phys. Rev. D **103**, 084031 (2021)
63. C. Zhang, A. Wang, T. Zhu, JCAP **05**, 059 (2023)
64. C. Zhang, T. Zhu, X. Fang, A. Wang, Phys. Dark Univ. **37**, 101078 (2022)
65. R. Haberman, (Pearson Education, One Lake Street, 2013)
66. J.M. Maldacena, A. Strominger, Phys. Rev. D **55**(861), 870 (1997)
67. M. Cvetic, F. Larsen, Phys. Rev. D **56**(4994), 5007 (1997)
68. S. Fernando, Gen. Rel. Grav. **37**(461), 481 (2005)
69. G. Panotopoulos, A. Rincon, Phys. Rev. D **97**, 085014 (2018)
70. W. Javed, M. Aqib, A. Övgön, Phys. Lett. B **829**, 137114 (2022)
71. M. Visser, Phys. Rev. A **59**(427), 438 (1999)
72. P. Boonserm, M. Visser, Phys. Rev. D **78**, 101502 (2008)
73. P. Boonserm, T. Ngampitipan, P. Wongjun, Eur. Phys. J. C **78**, 492 (2018)
74. Y. Yang et al., Phys. Rev. D **107**, 064042 (2023)
75. F. Gray, M. Visser, Universe **4**, 93 (2018)
76. T. Ngampitipan, P. Boonserm, Int. J. Mod. Phys. D **22**, 1350058 (2013)
77. S. Barman, Eur. Phys. J. C **80**, 50 (2020)
78. H. Xu, M.H. Yung, Phys. Lett. B **794**(77), 82 (2019)
79. M. Visser, Phys. Rev. A **59**(427), 438 (1999)
80. P. Boonserm, M. Visser, Phys. Rev. D **78**, 101502 (2008)

81. P. Boonserm, T. Ngampitipan, P. Wongjun, Eur. Phys. J. C **79**, 330 (2019)
82. S. Iyer, C.M. Will, Phys. Rev. D **35**, 3621 (1987)
83. J.P. Luminet, Astron. Astrophys. **75**(228), 235 (1979)
84. Y.X. Huang, S. Guo, Y. Liang, Y.H. Cui, Q.Q. Jiang, K. Lin, Chin. Phys. C **48**, 045102 (2024)